Chen and Ye
Chinese Journal of Mechanical Engineering (2024) 37:72
https://doi.org/10.1186/s10033-024-01054-0

Chinese Journal of Mechanical Engineering

ORIGINAL ARTICLE

Open Access

Path-Dependent Progressive Failure Analysis for 3D-Printed Continuous Carbon Fibre Reinforced Composites

Yuan Chen[1,2*] and Lin Ye[1,2]

Abstract

In order to predict the damage behaviours of 3D-printed continuous carbon fibre (CCF) reinforced composites, when additional short carbon fibre (SCF) composite components are employed for continuous printing or special functionality, a novel path-dependent progressive failure (PDPF) numerical approach is developed. First, a progressive failure model using Hashin failure criteria with continuum damage mechanics to account for the damage initiation and evaluation of 3D-printed CCF reinforced polyamide (PA) composites is developed, based on actual fibre placement trajectories with physical measurements of 3D-printed CCF/PA constituents. Meanwhile, an elastic-plastic model is employed to predict the plastic damage behaviours of SCF/PA parts. Then, the accuracy of the PDPF model was validated so as to study 3D-printed CCF/PA composites with either negative Poisson's ratio or high stiffness. The results demonstrate that the proposed PDPF model can achieve higher prediction accuracies in mechanical properties of these 3D-printed CCF/PA composites. Mechanism analyses show that the stress distribution is generally aggregated in the CCF areas along the fibre placement paths, and the shear damage and matrix tensile/compressive damage are the key damage modes. This study provides a new approach with valuable information for characterising complex 3D-printed continuous fibre-matrix composites with variable mechanical properties and multiple constituents.

Keywords 3D printing, Continuous carbon fibre, Modelling, Energy absorption, Negative Poisson's ratio

1 Introduction

Fibre reinforced composites and especially continuous carbon fibre (CCF) reinforced composites are well-established as advanced materials with excellent stiffness- and strength-to-weight ratios for a wide range of industrial applications [1, 2]. Conventional manufacturing technologies are sometimes inconvenient, expensive and even incapable for producing CCF composites of extraordinary configurations to satisfy new design purposes and requirements, while 3D printing technology (i.e., additive manufacturing) has become increasingly important and effective to easily achieve new CCF composites with complex configurations and constituents. However, unlike conventionally manufactured CCF composites, as mentioned, usually 3D-printed CCF composites not only have complex structural geometries but also nonuniform fibre paths with variable mechanical properties and multiple constituents, which impedes their effective modelling and analysis for engineering applications.

Currently, research work for modelling 3D-printed CCF composites is increasing but still limited, though numerical analysis demonstrates strong advantages for investigating structural/material responses and minimising experimental cost. For instance, macro-scale [3–5], meso-scale [6, 7] and multi-scale models [8–10] were utilised for the numerical modelling of 3D-printed CCF

*Correspondence:
Yuan Chen
chenyuan@sustech.edu.cn
[1] School of System Design and Intelligent Manufacturing (SDIM), Southern University of Science and Technology, Shenzhen 518055, China
[2] Shenzhen Key Laboratory of Intelligent Manufacturing for Continuous Carbon Fibre Reinforced Composites, Southern University of Science and Technology, Shenzhen 518055, China

composites. In this context, several recent studies have been attracting researchers' attention to simulations. For instance, Abadi et al. [11] used finite element analysis to characterise the performance of 3D-printed continuous fibre reinforced composites. Majko et al. [4] performed numerical approaches based on the commercial software ADINA to analyse 3D-printed composite laminates reinforced with different fibre categories, i.e., continuous aramid, carbon and glass fibres. Van de Werken et al. [5] developed a numerical model to calculate the damage condition based on Tsai-Wu failure indices of a 3D-printed CCF composite dog bone specimen under tensile loading. Zhang et al. [12, 13] simulated 3D-printed continuous fibre reinforced composite plates with a central hole when subjected to tension and shearing. Recently, Avanzini et al. [14] proposed an embedded-elements technique to simulate the 3D-printed composite parts with complex geometry realised by continuous fibres. A comparative study of the embedded-elements approach with conventional analytical or numerical methods for stiffness assessment was performed, showing an accurate prediction of stiffness with the additional ability to model complex fibre deposition patterns when using the embedded-elements approach. This approach may deal with the predictions for 3D printed composites with complex fibre paths but is only available within the elastic domain, i.e., for predicting the structure's stiffness.

Hence, numerical modelling of thermoplastic-matrix specimens reinforced with continuous fibres obtained by 3D printing, i.e., fused filament fabrication (FFF), is still in its infancy [15]. Besides, most designed continuous fibre paths are complicated and additional material components are sometimes essential for continuous printing or special functionality of 3D-printed CCF reinforced composites. This has led to variable mechanical properties and multiple constituents [16, 17], while few relevant reports on such modelling methods are available, especially when damage states and analyses were considered.

In this study, a path-dependent progressive failure (PDPF) approach is proposed to predict and characterise 3D-printed CCF reinforced polyamide (PA) composites, i.e., two topologically-designed CCF composite structures with particular properties: Negative Poisson's ratio and high stiffness. In these, short carbon fibre reinforced PA (SCF/PA) components are additional constituents. Numerical models are based on continuum damage mechanics for progressive failure analysis of 3D-printed CCF/PA composites. These are developed by defining the physical fibre placement trajectories as the longitudinal fibre directions within the CCF areas. An elastic-plastic failure model for SCF/PA components based on experimental characterisation is also performed. The prediction results, in terms of the stiffness, peak force and energy absorption of 3D-printed CCF composites, are experimentally and numerically validated.

2 Specimen Preparation and Experiments

Structures with specific performance can be usually acquired via topological design [18–20]. In this study, the specimens functionalised with either negative Poisson's ratio/auxetic performance or high stiffness were obtained based on topological and fibre placement design using CCFs, as reported in Ref. [21]. A Markforged® MII 3D printer was utilised to additively manufacture the CCF/PA functional composites where some areas were printed with SCF/PA (deposited with ± 45° configurations, i.e., + 45° and − 45°, alternatively) for the sake of continuous printing [17]. The final CCF printing trajectories for the specimens with negative Poisson's ratio and high stiffness are shown in Figure 1(a) and (b), respectively. The CCF/PA and SCF/PA filaments for 3D printing were commercially acquired from Markforged Inc. For the 3D-printed composites, the single-layer thickness was 0.125 mm to form 64 layers with a total thickness of 8 mm. The printing paths in each layer are the same as seen in Figure 1(a) or (b), except for the upper and bottom surface layers which were deposited with SCF/PA under a compulsory default setup in Markforged system.

Based on ASTM D638, tensile tests were conducted using an Instron 3366 universal testing machine with a quasi-static constant displacement rate of 5.0 mm/min and a strain gauge with a gauge length of 12.5 mm to measure the effective stress-strain relation of the 3D-printed SCF/PA composite materials (deposited in ±45° configurations).

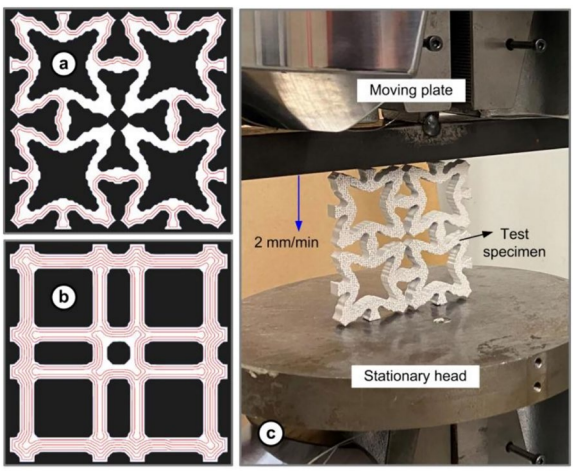

Figure 1 3D printing trajectories for CCF composites with (**a**) negative Poisson's ratio or (**b**) high stiffness, and (**c**) an auxetic specimen subjected to a compression test

Compression tests were conducted on the 3D-printed CCF reinforced specimens using an MTS 810 material testing machine with a data acquisition system to record the force-displacement curves. The displacement rate was set at 2.0 mm/min for all the compressive tests, as shown in Figure 1(c). During characterisation, the stiffness and peak force can be directly extracted while the energy absorption can be integrated from the force-displacement curve.

A digital image correlation (DIC) technique was employed to characterise the deformation and mechanical performance of the 3D-printed composites. For the DIC analysis, a white-coloured coating was sprayed on the surface of the planar lattice followed by the application of a uniform pattern of black dots applied using an embossed ink-covered roller. These black dots could be captured by the DIC camera to enable the determination of the displacements or strains. The accuracy of the measured displacement was approximately ±0.02%.

3 A Path-Dependent Progressive Failure Analysis

As mentioned before, the complex curvilinear fibre trajectories of 3D-printed continuous fibre composites, such as those shown in Figure 1(a) and (b), lead to variable mechanical properties which are difficult to be accurately modelled using a conventional progressive failure (CPF) model based on approximated fibre orientations with continuum damage mechanics [16, 22]. In this study, a novel numerical modelling method, i.e., a PDPF analysis model, is proposed and developed to predict and analyse the progressive failure response of 3D-printed CCF composites.

First, the actual fibre deposition trajectories are straightforwardly extracted from the Eiger system of the Markforged printer. Then, the basic width of consolidated CCF/PA filaments is experimentally measured and determined as shown in Figure 2(a), leading to a width value of around 0.72 mm for the 3D-printed CCF/PA in the fibre rich areas. The fibre rich area is where the fibre filaments are deposited back and forth without any gap and within which there are no other material parts (i.e., SCF/PA). Besides, the mechanical properties in the rich area are the same as those of 3D-printed CCF/PA standard tensile specimens that can be experimentally characterised, as reported in Refs. [23, 24].

Numerically, in this study, the volume of 3D-printed filaments is calculated based on the rectangular shaped 3D printed filaments other than the fact of oval-like shaped filaments by FFF. Taking the CCF composites with negative Poisson's ratio as an example, based on the basic fibre width of 0.72 mm and fibre trajectories of Figure 1(a), the areas of 3D-printed CCF/PA parts with their fibre placement directions can be determined as presented in

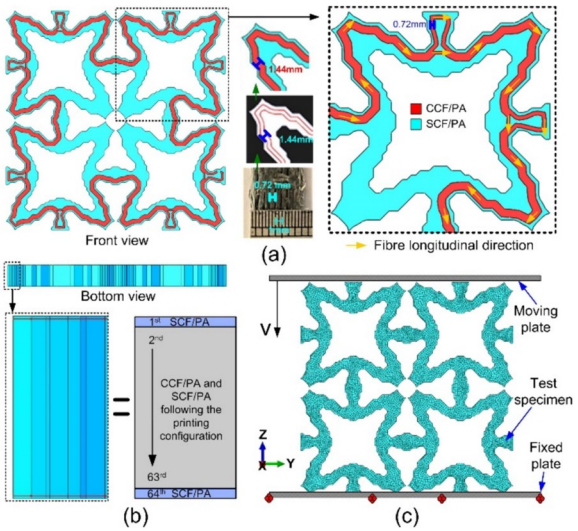

Figure 2 Numerical setup: (**a**) A front view of 3D-printed CCF composite structure with negative Poisson's ratio and determination of 3D-printed CCF/PA and SCF/PA parts, (**b**) A bottom view and through-thickness distribution of 3D-printed CCF/PA and SCF/PA parts, (**c**) Meshwork of a CCF/PA composite with boundary conditions

Figure 2(a), where the deposited two adjacent layers then lead to 1.44 mm width for numerical modelling. Meanwhile, the curved areas of 3D-printed CCF composites may possess a lower fibre volume fraction due to fibre loss during printing [25]. Therefore, the curved sections were generally reduced or marginally adjusted within a basic range of 0.6–0.85 mm based on experimental measurement of filament widths including those in fibre rich, curved and other areas, until the final volume of deposited CCF/PA filaments meets that given by the Eiger system.

3.1 Progressive Failure of 3D-Printed CCF/PA Composite

The damage behaviours of CCF composites are complicated. They comprise intralaminar damage, e.g., continuous fibre fracture/rupture, matrix cracking/crushing and interlaminar damage/delamination [26]. To date, continuum damage mechanics is of great advantage in calculating the intralaminar damage of CCF composites in a damage accumulation manner based on the damage variables ranging from 0 to 1, for the description of a damage initial state and the progressive development process. In the PDPF model, the orthogonal material constitutive equations were developed based on continuum elements in an Abaqus simulation platform, and the corresponding failure criteria were utilised for calculating the damage initiation and propagation. Among several failure criteria [27–31], one of the mostly utilised methods for unidirectional CCF composites, namely, Hashin criterion [28,

Table 1 Mechanical properties of 3D-printed CCF/PA composites [16, 24]

Properties	Variable	Value
Density (kg/m^3)	ρ	1250
Fibre volume (%)	V	31.4
Longitudinal Young's modulus (GPa)	E_{11}	69.4
Transverse Young's modulus (GPa)	E_{22}	3.5
Principal Poisson's ratio	v_{12}	0.33
Shear modulus (GPa)	G_{12}	1.9
Longitudinal tensile strength (MPa)	X_T	905.3
Longitudinal compressive strength (MPa)	X_C	426
Transverse tensile strength (MPa)	Y_T	17.9
Transverse compressive strength (MPa)	Y_C	66
In-plane shear strength (MPa)	S_{12}	43.4
Longitudinal traction fracture energy (kJ/m^2)	G^C_{ft}	91.6
Longitudinal compression fracture energy (kJ/m^2)	G^C_{fc}	79.9
Transverse traction fracture energy (kJ/m^2)	G^C_{mt}	0.22
Transverse compression fracture energy (kJ/m^2)	G^C_{mc}	1.1

29], was employed to predict the failure responses of the 3D-printed CCF composites.

Details for the constitutive equations and failure criteria for 3D-printed CCF/PA composites are presented in Appendix A. The basic mechanical properties were obtained from Refs. [16, 24] for the same 3D-printed CCF/PA composites, with a nominal CCF volume fraction of 31.4% and a void content of 7.5% [24]. With these previous characterisations, the basic mechanical properties are summarised in Table 1. In this study, the interlaminar damage/delamination was observed as an insignificant behaviour [16], hence the interfaces between the printed layers have not been taken into account.

As mentioned, in the PDPF model, the 3D-printed CCF/PA filaments in composite layers were calculated using orthotropic material constitutive properties, shown in Table 1, where the fibre longitudinal direction was defined along the CCF filament trajectories, i.e., as marked in Figure 2(a). Specifically, in Abaqus, the primary axis direction, i.e., the fibre longitudinal direction, as exhibited in Figure 2(a), was defined using an "Edges" option by choosing the CCF filament trajectories when setting up the orientation for composite layups, meanwhile the normal axis direction, i.e., the through-thickness direction was set along the x direction according to Figure 2, so the fibre transverse direction was then automatically determined since it is perpendicular to the longitudinal and through-thickness directions.

3.2 Elastic-Plastic Behaviour of SCF/PA Composite

As previously mentioned, SCF/PA was utilised as additional material components filling the space where CCF/PA placement was difficult in continuous printing, so once the CCF/PA placement areas have been determined using the approach as shown in Section 3.1, the remaining sections will be defined as SCF/PA composites for simulation. SCF/PA was selected because of its better performance than the PA counterpart [17]. As introduced in Section 2, the SCF/PA filament was placed in ±45° configurations in all printing, and the nominal volume fraction was ~10% [16], leading to an increment of elastic modulus of PA but providing no big improvement in tensile strength. Hence, for modelling purposes, it was treated as an isotropic material for numerical analysis, though it has minor orthotropy [16].

The mechanical properties of 3D-printed SCF/PA composites were specifically characterised in this study. According to ASTM D638, tensile tests were conducted for type IV dog bone SCF/PA specimens (deposited with ±45° path configurations), using a universal testing machine with a quasi-static constant velocity of 5.0 mm/min and a strain gauge with a gauge length of 10 mm to obtain the effective or engineering stress-strain relation.

The mean results of the experimental stress-strain curves of standard specimens produced by repetitive testing were extracted and converted into the true stress-strain curve for modelling [32], as shown in Figure 3. Then, an elastic-plastic model was established using the true stress-strain curve. A summary of its basic properties is depicted: The density is 1160 kg/m^3, tensile modulus is 898 MPa, tensile strength is 50 MPa and failure strain is 0.4. In failure analysis, the equivalent plastic strain (PEEQ) describing an accumulation of the plastic deformation during the process

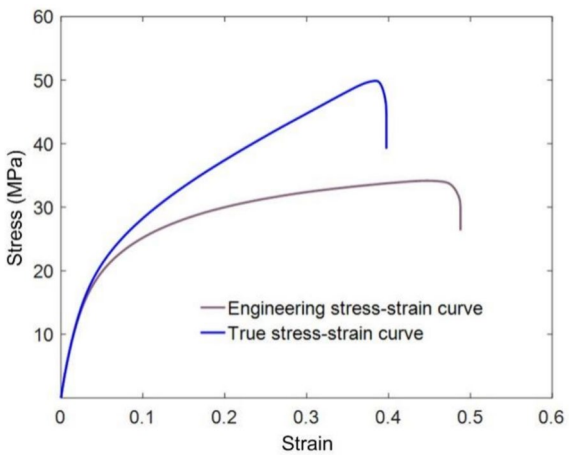

Figure 3 Experimental engineering and true stress-strain curves of 3D-printed SCF/PA specimens (deposited in ±45° configurations)

was utilised for characterising the plastic deformation. This was done because of PEEQ's wide applications with benefits for comprehensive and effective evaluation using a scalar rather than a complex strain tensor [33, 34]. In addition, a ductile criterion in Abaqus was applied to determine the final failure of SCF/PA materials using a predefined failure strain (=0.4) based on the elastic-plastic model, to exhibit the materials' fracture behaviour.

3.3 Numerical Definitions and Boundary Conditions

As shown in Figure 2(b), the through-thickness distribution of sixty-two layers of 3D-printed CCF/PA with additional SCF/PA parts and two layers of complete SCF/PA was numerically built, where the two SCF/PA layers of the upper and bottom surfaces are compulsory options because of using the Markforged printer. Hence, the specimens consisted of sixty-four plies and each ply had the same thickness of 0.125 mm, based on the printing setup. In each layer, the continuous fibre longitudinal directions, as mentioned, were defined to be the same as those of printing trajectories as shown in Figure 1(a). With the Markforged printer, there is one single wall of SCF/PA, as the casing around a printed profile, which was ignored in the simulation, due to its very limited volume fraction and insignificant effects on characterisation.

The numerical models were developed using Abaqus/Explicit to calculate the structural responses and materials failure. Under compression, 8-node quadrilateral continuum shell elements (SC8R) were applied for the 3D-printed composites to guarantee accurate modelling and to improve the calculation's efficiency [2]. The moving and fixed plates were modelled with conventional shell elements (S4R). After a convergence study on mesh and velocity, a constant displacement rate of 100 mm/s was applied for the moving plate (so that the dynamic effect would be insignificant when the velocity was below 500–1000 mm/s [2] to improve the calculation efficiency) and a uniform mesh with the element size of 0.9 mm was used for modelling the 3D-printed specimens [16].

The meshwork of 3D-printed CCF/PA auxetic composite and specific boundary conditions are exhibited in Figure 2(c). A general contact algorithm was deployed to calculate and simulate the general interaction between the elements [32]. The friction coefficients for the contact interfaces were generally defined as 0.3. During the simulation, in accordance with the failure criteria for CCF/PA and the failure strain for SCF/PA, the totally failed elements were removed for further calculation. The same numerical definitions were performed for modelling the high stiffness 3D-printed CCF composites.

4 Results and Discussion

4.1 Case Study 1: Auxetic Composites

The first case is a 3D-printed auxetic composite with fibre deposition trajectories as shown in Figure 1(a) and subjected to in-plane compression as introduced previously. The absolute fibre volume fraction is 3.7% [21]. The experiments show that these CCF/PA composite structures demonstrate a negative Poisson's ratio from − 0.2 to − 0.1 as the compression displacement progresses from 0 mm to 4 mm within the effective displacement [16] (so the DIC photographic analysis and numerical modelling were performed at 4 mm).

Their force-displacement curves are presented in Figure 4. We can see that the force increases from zero to around 500 N where the surfaces of upper and bottom unit cells were contacted at about 2 mm, then the force is further increased to peak at about 2000 N, and afterwards it gradually decreases when the compressive displacement is over 4 mm. In comparison, the predicted force-displacement curve of the PDPF model agrees well with those of experiments, though discrepancies can be also captured. The reasons can be concluded as follows: the ignorance of the practical interface properties between CCF/PA and SCF/PA sections and the materials' orthotropic characteristics during modelling for SCF/PA materials. Additionally, the discrepancies can be also attributed from the initial stress and fibre damage in experimental specimens when there were 3D-printed curved sections [16]. Basically, the models are acceptable in predicting the key mechanical features of 3D-printed CCF composite structures.

The compression behaviours captured for horizontal displacement, i.e., the displacement along the x direction, U_{xx}, by DIC and simulation at Point B of 4 mm are depicted on the right-hand side of Figure 4. It can be found that when the compression displacement is 4 mm, the structure undergoes a horizontal shrinkage along the

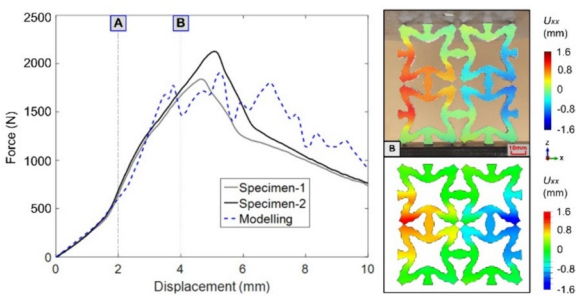

Figure 4 Comparison of force-displacement curves and horizontal displacement U_{xx} by DIC photographic analysis (upper) and simulation (bottom) at Point B of 4 mm for 3D-printed CCF/PA auxetic composites

x direction, where its left and right parts deform positively and negatively, respectively, indicating an evident auxetic behaviour in both experiments and simulation.

Based on experimental/numerical observation and force-displacement curves of Figure 4, the CCF/PA specimen has already been failed and is about to confronting out-of-plane bending behaviour which is not our focus, so the investigation is performed within 4 mm of Point B. Then, the deformation and damage process before 4 mm captured by DIC photographic analysis of horizontal strain by experiments and von Mises stress by simulation for 3D-printed CCF/PA auxetic composites are shown in Figure 5. The DIC results demonstrate that, as the plate compresses to Point B, both positive and negative horizontal strain ε_{xx} are intersectionally aggregated in the CCF/PA auxetic composites, contributing to their auxetic behaviours. Accordingly, from the stress analysis and CCF trajectories presented in Figure 1(a), it can be seen that Mises stresses are mainly concentrated in the CCF areas along the fibre placement paths, especially in those vertical CCFs against the compression loading, where the maximum stress is 283.9 MPa when the displacement is 4 mm. During the compression process, the stress/strain analyses at the marked circles in Figure 5 show that the material failure locally occurs at ligaments within each unit cell along the vertical CCF trajectories.

Further, failure mechanism analyses were performed for 3D-printed CCF/PA auxetic composite with respect to the CCF/PA damage characteristics (Hashin criteria) and SCF/PA plastic deformations (PEEQ) at displacement Point B of 4 mm when under in-plane compression. The results are shown in Figure 6. It is found that fibre damage is not predominant for the 3D-printed CCF/PA auxetics. Shear damage and matrix tensile/compressive damage can be observed at the ligaments within each unit cell, which is attributed to the auxetic behaviours of each unit cell under compression. In terms of the plastic deformation for the SCF/PA parts, slight damage is observed at local contact areas near the moving and fixed plates.

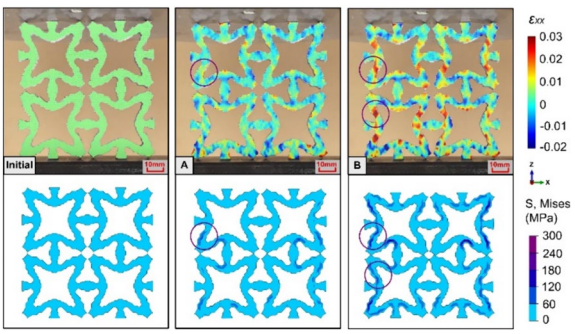

Figure 5 Deformation and damage process captured by DIC photographic analysis of horizontal strain ε_{xx} by experiments and von Mises stress by simulation for 3D-printed CCF/PA auxetic composites

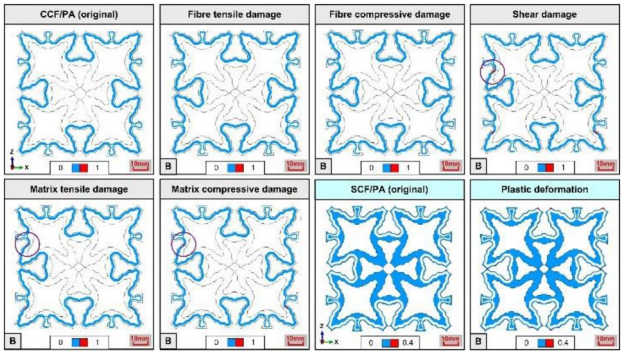

Figure 6 Failure mechanisms in terms of CCF/PA damage and SCF/PA deformation at displacement Point B of 4 mm for 3D-printed CCF/PA auxetic composite

In order to investigate the mechanical performance and model effectiveness for the 3D-printed CCF/PA auxetic composite under in-plane compression, its stiffness, peak force and energy absorption calculated by experiments, PDPF model and CPF model are shown in Figure 7. By experiments, the (mean) stiffness of 3D-printed CCF/PA composite auxetics is 219.7 N/mm, while the predicted results by the PDPF and CPF models are 254.4 N/mm and 289 N/mm, respectively. This indicates that the accuracy using the PDPF model has been improved by 16% as compared to that using the CPF model. The peak forces predicted by PDPF and CPF models are almost at the same level, with a variation of − 3.9% and 3.5%, respectively, from the experimental (mean) peak force of 1982.6 N. Finally, the (mean) energy absorption of 3D-printed CCF/PA auxetic was experimentally measured as 10.6 J, which is 10.8% and 13.4% smaller than those predicted by PDPF and CPF models, respectively. Therefore, the accuracy using the PDPF method has been enhanced by 2.6%. Apparently, the PDPF model is more accurate in the prediction of mechanical performance of 3D-printed auxetic composites.

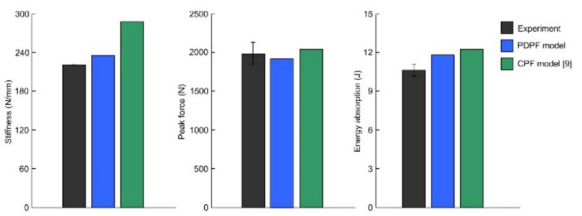

Figure 7 Mechanical performance and model effectiveness for the 3D-printed CCF/PA auxetic composite in terms of stiffness, peak force and energy absorption

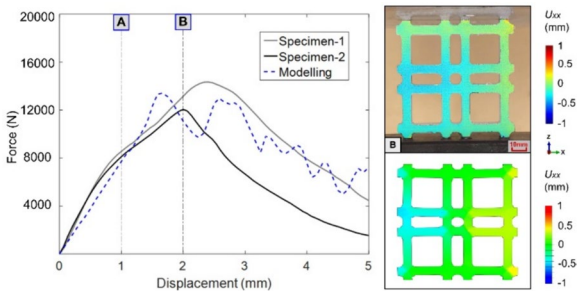

Figure 8 Comparison of force-displacement curves and horizontal displacement U_{xx} by DIC photographic analysis (upper) and simulation (bottom) at Point B of 2 mm for 3D-printed CCF/PA high stiffness composites

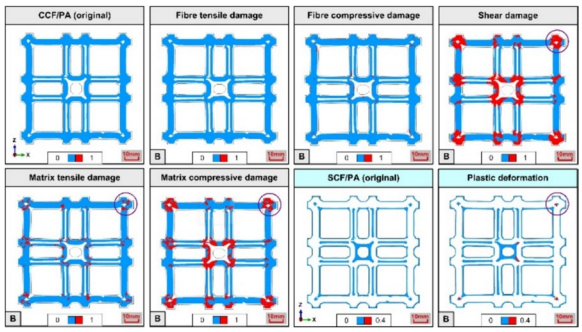

Figure 10 Failure mechanisms in terms of CCF/PA damage and SCF/PA deformation at displacement Point B of 2 mm for 3D-printed CCF/PA high stiffness composite

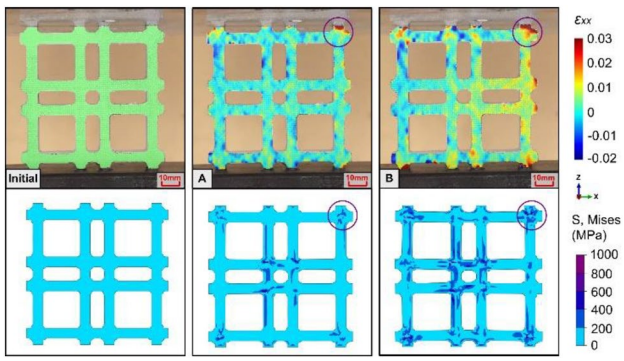

Figure 9 Deformation and damage process captured by DIC photographic analysis of horizontal strain ε_{xx} by experiments and von Mises stress by simulation for 3D-printed CCF/PA high stiffness composites

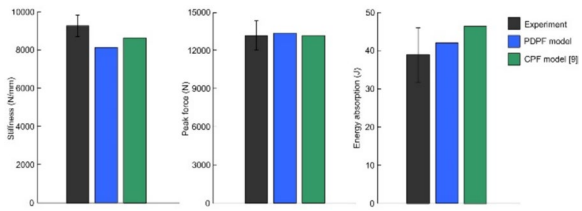

Figure 11 Mechanical performance and model effectiveness for the 3D-printed CCF/PA high stiffness composite in terms of stiffness, peak force and energy absorption

4.2 Case Study 2: High Stiffness Composites

The second case is a topologically-designed 3D-printed CCF/PA high stiffness composite with a structural configuration and fibre placement trajectories as shown in Figure 1(b). The basic structural size (80 mm×80 mm×8 mm) and boundary conditions were the same as those of CCF/PA auxetic composites. The absolute fibre volume fraction is 7.6% [21]. By experiments and simulation, the compressive force-displacement curves with the compressive responses of 3D-printed CCF/PA high stiffness composites are shown in Figure 8. The force of CCF/PA has a rapid increment to over 12000 N before the displacement is 2 mm; subsequently, the force decreases steadily to below 6000 N. In comparison, the force propagation trend is well predicted by the PDPF model. The horizontal displacement by DIC photographic analysis and simulation at Point B of 2 mm for 3D-printed CCF/PA high stiffness composites is also presented in Figure 8, where both DIC and simulation results show severe negative and positive displacements on the left and right edges, respectively, along the horizontal direction, demonstrating the structures' apparent expansion behaviour.

As well, the CCF/PA specimen with out-of-plane bending behaviour after the displacement reaches 2 mm is not concentrated, such that the study is performed within 2 mm. By observation of the compressive behaviours, i.e., the deformation and damage process, as shown in Figure 9, the local strain concentration can be seen at the contact areas nearing the plates as denoted by the marked circles, which is also reflected by the stress distribution in the simulation results, as especially when the compression continues from Point A to B. In addition, the stress distribution is generally aggregated in the CCF areas along the fibre placement paths, with the maximum stress reaching 904.7 MPa when the displacement is 2 mm at Point B.

As shown in Figure 10, failure analyses show that the shear damage and matrix tensile/compressive damage are still the key damage mechanisms for CCF/PA parts. However, the damage magnitude of the 3D-printed CCF/PA high stiffness composite is much more severe than that of the CCF/PA auxetic composite. Further, the damage mainly occurred at the four corners and central area, where either fibre shortage or discontinuity generally existed, as indicated by the fibre trajectories shown in Figure 1(b). While the plastic deformation is

also basically located around the four corners and the central area, it is locally concentrated with insignificant distributions.

The mechanical performance of 3D-printed CCF/PA high stiffness composites by experiments and simulation are presented in Figure 11. The (mean) stiffness and peak force in experiments are 9301.7 N/mm and 13197.2 N, respectively, which are accordingly around 10% and under 2% of difference to those predicted using either PDPF or CPF model. However, the experimental (mean) energy absorption is 38.5 J, with a variation of 9.5% and 21.6% from those predicted by the PDPF and CPF models, respectively, indicating that the modelling accuracy is improved by 12% when using the PDPF model. The conclusion can be drawn that the PDPF model has higher modelling accuracy than the CPF model for 3D-printed CCF composites.

5 Conclusions

(1) A PDPF analysis method using the orthogonal material constitutive relations with continuum damage mechanics was developed to predict the damage initiation and evaluation of 3D-printed CCF/PA composites. Two cases on 3D-printed CCF/PA composites, one with negative Poisson's ratio and the other with high stiffness were calculated for validation and characterisation.

(2) The results demonstrated that the PDPF model can well predict not only the force-displacement curves but also the damage behaviours of multiple constituents, i.e., CCF/PA and SCF/PA, in both cases. Besides, as compared to the CPF modelling method, the current PDPF model generally had higher prediction accuracies, such as a 16% and 12% improvement in the prediction of the stiffness of 3D-printed CCF/PA composite auxetics and the energy absorption of 3D-printed CCF/PA high stiffness composites, respectively.

(3) Mechanism analyses showed that the stress distribution was generally aggregated in the CCF areas along the fibre placement paths, and the shear damage and matrix tensile/compressive damage were the key damage mechanisms for both 3D-printed CCF/PA auxetic and high stiffness composites. However, the damage magnitude of the 3D-printed CCF/PA high stiffness composite was much more severe than that of the CCF/PA auxetic composite. In contract, plastic deformation was basically locally concentrated with insignificant distributions.

(4) In this study, we established and proved a new effective modelling method for 3D-printed CCF/PA composites, providing valuable choices and information for predicting continuous fibre-matrix composites with complex fibre paths, variable mechanical properties and multiple constituents. This model should be also available for the prediction of those continuous fibre-matrix composites made by other manufacturing techniques, e.g., vacuum assisted resin infusion (VARI) processing.

Appendix

Progressive Failure Criteria for Modelling 3D-Printed CCF/PA Composites

When modelling the continuous fibre, i.e., CCF/PA composites, the material constitutive relations is presumed to be a plane stress orthotropic material with linear elasticity, by which the constitutive response of the material can be calculated based on continuum damage mechanics as follows:

$$\boldsymbol{\sigma} = \boldsymbol{C_d}\boldsymbol{\varepsilon}, \tag{A1}$$

where $\boldsymbol{\varepsilon}$ is the elastic strain and $\boldsymbol{\varepsilon} = (\varepsilon_{11}, \varepsilon_{22}, \varepsilon_{12})^{\mathrm{T}}$, $\boldsymbol{\sigma}$ is the stress vector and $\boldsymbol{\sigma} = (\sigma_{11}, \sigma_{22}, \sigma_{12})^{\mathrm{T}}$, and $\boldsymbol{C_d}$ is the damage-variable based stiffness matrix,

$$\boldsymbol{C_d} = \frac{1}{D}\begin{bmatrix} (1-d_f)E_{11} & (1-d_f)(1-d_m)\nu_{21}E_{11} & 0 \\ (1-d_f)(1-d_m)\nu_{12}E_{22} & (1-d_m)E_{22} & 0 \\ 0 & 0 & (1-d_s)G_{12}D \end{bmatrix}, \tag{A2}$$

where d_f, d_m and $d_s = 1-(1-d_f)(1-d_m)\nu_{12}\nu_{21}$ are the continuous fibre, matrix and shear damage variables, respectively, varying from 0 (undamaged) to 1 (completely damaged) to reflect the material modulus degradation. E_{11}, E_{22} and G_{12} are the Young's moduli while ν_{12} and ν_{21} are the Poisson ratios. Thus, the damage variables determine the reduction of elastic properties and influence the stress propagation and residual strength in the plies. For the failure calculation, based on Hashin's method [28, 29], the initiation failure criteria in the progressive failure modelling are presented below.

Once any the four failure initiation modes in Table 2 have been reached, the corresponding damage are evaluated by calculating equivalent stress and strain in a linear degradation as follows.

Fibre tension ($\sigma_{11} \geq 0, \varepsilon_{11} \geq 0$):

$$\delta_{eq}^{ft} = L_c\sqrt{\langle\varepsilon_{11}\rangle^2 + \alpha\varepsilon_{12}^2}, \quad \sigma_{eq}^{ft} = \frac{\langle\sigma_{11}\rangle\langle\varepsilon_{11}\rangle + \alpha\sigma_{12}\varepsilon_{12}}{\delta_{eq}^{ft}/L_c}. \tag{A3}$$

Table 2 Hashin damage initiation criteria for 3D-printed CCF/PA composites in the modelling

Description	Stress condition	Damage initiation
Fibre tensile mode	$\sigma_{11} \geq 0$	$F_{ft} = \left(\frac{\sigma_{11}}{X_T}\right)^2 + \alpha\left(\frac{\sigma_{12}}{S_{12}^L}\right)^2$
Fibre compressive mode	$\sigma_{11} \leq 0$	$F_{fc} = \left(\frac{\sigma_{11}}{X_C}\right)^2$
Matrix tensile mode	$\sigma_{22} \geq 0$	$F_{mt} = \left(\frac{\sigma_{22}}{Y_T}\right)^2 + \left(\frac{\sigma_{12}}{S_{12}^L}\right)^2$
Matrix compressive mode	$\sigma_{22} \leq 0$	$F_{mc} = \left(\frac{\sigma_{22}}{2S_{12}^T}\right)^2 + \left[\left(\frac{Y_C}{2S_{12}^T}\right)^2 - 1\right]\frac{\sigma_{22}}{Y_C} + \left(\frac{\sigma_{12}}{S_{12}^L}\right)^2$

Note: X_T and X_C are the strengths along the fibre direction under uniaxial tensile and compressive loading, respectively; Y_T and Y_C are the strengths of the matrix normal to the fibre direction under uniaxial tensile and compressive loading, respectively; S_{12}^L and S_{12}^T denote shear strengths in the longitudinal and transverse directions, respectively with $S_{12}^L = S_{12}^L = S_{12}$; α is the coefficient determining the contribution of shear stress to the fibre tensile mode and it is defined as 1 to fully include shear stress; F_{ft}, F_{fc}, F_{mt} or F_{mc} are the assessment values, by which if it is equal to or higher than 1, the damage initiation criteria are met and afterwards the damage evaluation process will begin.

Fibre compression ($\sigma_{11} < 0, \varepsilon_{11} < 0$):

$$\delta_{eq}^{fc} = L_c\langle -\varepsilon_{11}\rangle, \quad \sigma_{eq}^{fc} = \frac{\langle -\sigma_{11}\rangle\langle -\varepsilon_{11}\rangle}{\delta_{eq}^{fc}/L_c}. \tag{A4}$$

Matrix tension ($\sigma_{22} \geq 0, \varepsilon_{22} \geq 0$):

$$\delta_{eq}^{mt} = L_c\sqrt{\langle\varepsilon_{22}\rangle^2 + \varepsilon_{12}^2}, \quad \sigma_{eq}^{mt} = \frac{\langle\sigma_{22}\rangle\langle\varepsilon_{22}\rangle + \sigma_{12}\varepsilon_{12}}{\delta_{eq}^{mt}/L_c}. \tag{A5}$$

Matrix compression ($\sigma_{22} < 0, \varepsilon_{22} < 0$):

$$\delta_{eq}^{mc} = L_c\sqrt{\langle -\varepsilon_{22}\rangle^2 + \varepsilon_{12}^2}, \quad \sigma_{eq}^{mc} = \frac{\langle -\sigma_{22}\rangle\langle -\varepsilon_{22}\rangle + \sigma_{12}\varepsilon_{12}}{\delta_{eq}^{mc}/L_c}, \tag{A6}$$

where L_c, the characteristic length, is determined by the element geometry and introduced to normalise the elements with different size ranges and ε_{11}, ε_{22} and ε_{12} are the elastic strain. Accordingly, such a bilinear equivalent stress-strain model for the failure initiation and evolution of the 3D-printed CCF/PA composites is then applied with continuum damage mechanics in current modelling.

Acknowledgements
The authors appreciate the invitation from professor Shan-tung Tu and professor Guoyan Zhou for submission of our research work to *Chinese Journal of Mechanical Engineering*.

Authors' Contributions
YC and LY were in charge of the whole trial; YC and LY wrote the manuscript; YC assisted with sampling and laboratory analyses. All authors read and approved the final manuscript.

Funding
Supported by National Natural Science Foundation of China (Grant No. 12302177), Guangdong Provincial Basic and Applied Basic Research Foundation of China (Grant No. 2024A1515010203), Shenzhen Science and Technology Program of China (Grant No. JCYJ20230807093602005), Shenzhen Key Laboratory of Intelligent Manufacturing for Continuous Carbon Fibre Reinforced Composites of China (Grant No. ZDSYS20220527171404011).

Data availability
Data will be made available on request.

Declarations

Competing Interests
The authors declare no competing financial interests.

Received: 1 February 2022 Revised: 29 May 2024 Accepted: 6 June 2024
Published online: 23 July 2024

References

[1] Y Sun, Z B Cai, S B Wu, et al. Effect of cycling low velocity impact on mechanical and wear properties of CFRP laminate composites. *Chin. J. Mech. Eng.*, 2018, 31: 112.
[2] Y Chen, L Ye, K K Fu. Progressive failure of CFRP tubes reinforced with composite sandwich panels: Numerical analysis and energy absorption. *Compos. Struct.*, 2021, 263: 113674.
[3] M Galati, M Viccica, P Minetola. A finite element approach for the prediction of the mechanical behaviour of layered composites produced by continuous filament fabrication (CFF). *Polym. Test.*, 2021, 98: 107181.
[4] J Majko, M Saga, M Vasko, et al. FEM analysis of long-fibre composite structures created by 3D printing. *Transportation Research Procedia*, 2019, 40: 792–799.
[5] N Van de Werken, J Hurley, P Khanbolouki, et al. Design considerations and modeling of fiber reinforced 3D-printed parts. *Compos. Part B Eng.*, 2019, 160: 684–92.
[6] E Zappino, M Filippi, A Pagani, et al. Experimental and numerical analysis of 3D printed open-hole plates reinforced with carbon fibers. *Composites Part C: Open Access*, 2020, 2: 100007.
[7] S Sangaletti, I G García. Fracture tailoring in 3D printed continuous fibre composite materials using the phase field approach for fracture. *Compos. Struct.*, 2022, 300: 116127.
[8] E Polyzos, D Van Hemelrijck, L Pyl. Modeling elastic properties of 3D printed composites using real fibers. *Int. J. Mech. Sci.*, 2022, 232: 107581.
[9] Y T Fu, X F Yao. Multi-scale analysis for 3D printed continuous fiber reinforced thermoplastic composites. *Compos. Sci. Technol.*, 2021, 216: 109065.
[10] Y T Fu, Y Kan, X Fan, et al. Novel designable strategy and multi-scale analysis of 3D printed thermoplastic fabric composites. *Compos. Sci. Technol.*, 2022, 222: 109388.

[11] H A Abadi, H T Thai, V Paton-Cole, et al. Elastic properties of 3D-printed fibre-reinforced structures. *Compos. Struct.*, 2018, 193: 8–18.
[12] H Q Zhang, D M Yang, Y Sheng. Performance-driven 3D printing of continuous curved carbon fibre reinforced polymer composites: A preliminary numerical study. *Compos. Part B Eng.*, 2018, 151: 256–64.
[13] H Q Zhang, A N Dickson, Y Sheng, et al. Failure analysis of 3D-printed woven composite plates with holes under tensile and shear loading. *Compos. Part B Eng.*, 2020, 186: 107835.
[14] A Avanzini, D Battini, L Giorleo. Finite element modelling of 3D printed continuous carbon fiber composites: Embedded elements technique and experimental validation. *Compos. Struct.*, 2022, 292: 115631.
[15] E Polyzos, D V Hemelrijck, L Pyl. Numerical modelling of the elastic properties of 3D-printed specimens of thermoplastic matrix reinforced with continuous fibres. *Compos. Part B Eng.*, 2021, 211: 108671.
[16] Y Chen, L Ye, Y X Zhang, et al. Compression behaviours of 3D-printed CF/PA metamaterials: Experiment and modelling. *Int. J. Mech. Sci.*, 2021, 206: 106634.
[17] Y Chen, L Ye. Topological design for 3D-printing of carbon fibre reinforced composite structural parts. *Compos. Sci. Technol.*, 2021, 204: 108644.
[18] B L Zhu, X M Zhang, M Liu, et al. Topological and shape optimization of flexure hinges for designing compliant mechanisms using the level set method. *Chin. J. Mech. Eng.*, 2019, 32: 13.
[19] J Gao, M Xiao, Y Zhang, et al. A comprehensive review of isogeometric topology optimization: Methods, applications and prospects. *Chin. J. Mech. Eng.*, 2020, 33: 87.
[20] Y Chen, L Ye, C Xu, et al. Multi-material topology optimisation of microcomposites with reduced stress concentration for optimal functional performance. *Mater. Design.*, 2021, 210: 110098.
[21] Y Chen, L Ye. Designing and tailoring effective elastic modulus and negative Poisson's ratio with continuous carbon fibres using 3D printing. *Compos. Part A Appl. Sci. Manuf.*, 2021, 150: 106625.
[22] Y L He, J P Davim, H Q Xue. 3D progressive damage based aacro-mechanical FE simulation of machining unidirectional FRP composite. *Chin. J. Mech. Eng.*, 2018, 31: 51.
[23] Q He, Z Y Man, L Chang, et al. On structure-mechanical and tribological property relationships of additive manufactured continuous carbon fiber/polymer composites. *Structure and Properties of Additive Manufactured Polymer Components. Woodhead Publishing*, 2020.
[24] M Iragi, C Pascual-González, A Esnaola et al. Ply and interlaminar behaviours of 3D-printed continuous carbon fibre reinforced thermoplastic laminates; Effects of processing conditions and microstructure. *Addit. Manuf.*, 2019, 30: 100884.
[25] H Shiratori, A Todoroki, M Ueda, et al. Compressive strength degradation of the curved sections of 3D-printed continuous carbon fiber composite. *Compos. Part A Appl. Sci. Manuf.*, 2021, 142: 106244.
[26] X Wang, X Y Tian, Q Lian, et al. Fiber traction printing: A 3D printing method of continuous fiber reinforced metal matrix composite. *Chin. J. Mech. Eng.*, 2020, 33: 31.
[27] S W Tsai. Strength theories of filamentary structures fundamental aspects of fibre reinforced plastic composites. *New York: Wiley-Interscience*, 1968: 3–11.
[28] Z Hashin, A Rotem. A fatigue failure criterion for fiber reinforced materials. *J. Compos. Mater.*, 1973, 7: 448–64.
[29] Z Hashin. Failure criteria for unidirectional fiber composites. *J. Appl. Mech.*, 1980, 47(2): 329–34.
[30] J P Hou, N Petrinic, C Ruiz, et al. Prediction of impact damage in composite plates. *Compos. Sci. Technol.*, 2000, 60(2): 228–73.
[31] A Puck, H Schürmann. Failure analysis of FRP laminates by means of physically based phenomenological models. *Compos. Sci. Technol.*, 2002, 62: 1633–62.
[32] Y Chen, L Ye, X Han. Experimental and numerical investigation of zero Poisson's ratio structures achieved by topological design and 3D printing of SCF/PA. *Compos. Struct.*, 2022, 293: 115717.
[33] J Y Zheng, X Y Shu, Y Z Wu, et al. Investigation on the plastic deformation during the stamping of ellipsoidal heads for pressure vessels. *Thin. Wall. Struct.*, 2018, 127: 135–144.
[34] F K Xia, T X Yu, Y Durandet, et al. Triangular corrugated sandwich panels under longitudinal bending. *Thin. Wall. Struct.*, 2021, 169: 108359.

Yuan Chen was an ARC postdoctoral research associate at *University of Sydney, Australia,* and currently he is an assistant professor at *Southern University of Science and Technology, China*. He obtained his PhD degree from *University of Sydney, Australia,* in 2019. His research interests are concentrated on additive manufacturing of composite materials, design and computational analysis of composite structures, topological and structural optimisation for metamaterials and advanced composites.

Lin Ye (a fellow of *Australian Academy of Technology and Engineering*) is currently a chair professor at *School of System Design and Intelligent Manufacturing (SDIM)*, *Southern University of Science and Technology, China*. His research interests include composites science and technology, smart materials & structures, structural integrity and durability.